Colloids and Surfaces A: Physicochemical and Engineering Aspects 657 (2023) 130569

Contents lists available at ScienceDirect

Colloids and Surfaces A: Physicochemical and Engineering Aspects

journal homepage: www.elsevier.com/locate/colsurfa

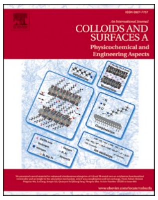

Comparison of turbulent drop breakup in an emulsification device and homogeneous isotropic turbulence: Insights from numerical experiments

Peyman Olad [a], Fredrik Innings [a,b], Marco Crialesi-Esposito [c], Luca Brandt [c,d], Andreas Håkansson [a,*]

[a] *Department of Food Technology, Engineering and Nutrition. Lund University, SE-221 00 Lund, Sweden*
[b] *Tetra Pak Processing Systems AB, SE-223 55 Lund, Sweden*
[c] *FLOW, Department of Engineering Mechanics, Royal Institute of Technology (KTH), SE-100 44 Stockholm, Sweden*
[d] *Department of Energy and Process Engineering, Norwegian University of Science and Technology (NTNU), NO-7491 Trondheim, Norway*

GRAPHICAL ABSTRACT

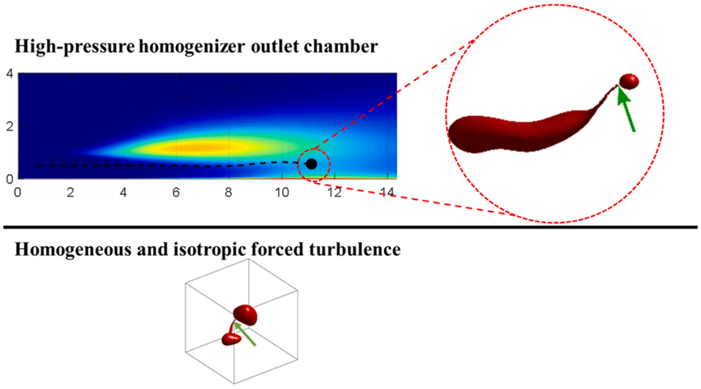

ARTICLE INFO

Keywords:
High-pressure homogenizer
Emulsification
Turbulence
Direct numerical simulation

ABSTRACT

Turbulent emulsification is of considerable industrial interest. Nevertheless, numerical experiments (direct numerical simulations, DNS, with highly resolved interface tracking) have been mainly used to study drop breakup in idealized flows. This study, therefore, compares drop breakup in two different settings (homogenous and isotropic flow, and a simplified high-pressure homogenizer) with the intention of better understanding how insight gained from the idealized systems can be applied to industrially relevant devices. The flow differs between the two cases, with highly anisotropic and inhomogeneous turbulence in the latter. Results show similarities between the two cases regarding morphology of breakup, suggesting that the underlying mechanism, as a function of Weber number, is similar. However, differences are also observed, e.g., in terms of breakup time and deformed morphology, which are associated with the locality of the turbulence in the homogenizer. Implications for an improved understanding of turbulent breakup in industrially relevant devices are discussed.

Abbreviations: DNS, Direct numerical simulation; HPH, High-pressure homogenizer; TKE, Turbulent kinetic energy; VOF, Volume of fluid.

[*] Corresponding author.

E-mail address: andreas.hakansson@food.lth.se (A. Håkansson).

https://doi.org/10.1016/j.colsurfa.2022.130569
Received 26 August 2022; Received in revised form 8 November 2022; Accepted 11 November 2022

Nomenclature

Latin

A	Interfacial area of the drop, m^2.
A_0	Interfacial area of the spherical drop (of diameter D_0), m^2.
D	Drop diameter, m.
D_0	Initial drop diameter, m.
f_2	Characteristic frequency, s^{-1}.
h	Gap height, m.
N	Number of computational cells, -.
Re_λ	Taylor-scale Reynolds number, -.
t	Time, s.
t_B	First effective breakup time, s.
t_{IB}	Initial breakup time, s.
U_j	Jet inlet bulk velocity, m s^{-1}.
We	Weber number, -.
x, y, z	Spatial dimensions (see Fig. 1), m.
Δx	Spatial resolutions (in x-dimension), m.

Greek

β_2	Dampening rate, s^{-1}.
γ	Interfacial tension, N m^{-1}.
ε	Dissipation rate of TKE, m^2 s^{-3}.
η	Kolmogorov length-scale, m.
ρ_C	Density of the continuous phase, kg m^{-3}.
τ_η	Kolmogorov time-scale, s.
$\tau_{\eta,0}$	Kolmogorov time-scale (at time of injection), s.

1. Introduction

Emulsification devices are essential in many applications where creating a dispersion of two immiscible liquids, i.e. an emulsion, is required. Emulsification is of special relevance for food industry since many foods are emulsions (e.g., dairy products, dressings and sauces) [1, 2]. Ensuring a high physical stability, as well as controlling structure, texture and appearance, requires efficient emulsification. Typically, a high-pressure homogenizer (HPH) is used for low to intermediate viscosity ratio emulsions; however, for applications with a higher viscosity ratio, a rotor-stator mixer is more favorable.

Regardless of which of these emulsification devices are chosen, the typical flow pattern where breakup takes place is a turbulent near-wall jet [3]. In rotor-stator mixers, breakup is observed in the turbulent jet clinging to and extending from the stator hole [4,5]. In HPH valves, a turbulent jet is created downstream of the narrow gap. This jet later bends and clings to the outlet chamber wall [6]. High-speed visualization experiments show drop breakup taking place at a distance of 5–20 gap heights downstream of the gap exit [6–9]. This corresponds to positions where the turbulent kinetic energy (TKE), created as large structures at the gap exit, has been transported to turbulent eddies of sizes comparable to the drops [10].

A growing number of experimental high-speed visualization studies are being performed to investigate single drop breakup in turbulent flows [11-21]. These studies have greatly increased the understanding of turbulent breakup, e.g., in term of breakup probabilities, the number of fragments formed per breakup, breakup rates, breakup times and drop size distributions. However, experimental visualization techniques also have limitations, e.g., in allowing for a relatively low temporal resolution and, typically but not exclusively [16,18], only measuring a two-dimensional projection of the drop (as opposed to a full three dimensional view).

In the last two decades, with the advances in computational power and numerical tools, numerical techniques have also been made available to study drop breakup. A growing number of studies are investigating turbulent drop breakup using direct numerical simulation (DNS) coupled with highly resolved interface tracking algorithms, often referred to as 'numerical drop breakup experiments'; a review is available elsewhere [22]. These techniques offer a valuable supplement to the experimental high-speed visualization studies, for example in clarifying turbulence modulation, breakup time and morphology, as well as the mechanism of turbulence-drop interactions [23-33].

Some investigations have been carried out using numerical breakup experiments in channel turbulence [34-37] and shear flow turbulence [38,39]. However, the majority of numerical drop breakup experiments are carried out in idealized flow conditions, i.e., homogenous and isotropic turbulence generated by synthetic forcing. No numerical breakup experiments have yet, to the best of the authors' knowledge, been conducted on emulsification devices. In particular, the turbulent flow field inside an emulsification device (such as an HPH or a rotor-stator mixer) is strongly anisotropic and inhomogeneous. Recent investigations suggest that the extent of anisotropy in the effective breakup region of an emulsification device has a substantial influence on the fragmentation frequency [40]. A drop traveling through the strongly anisotropic flow of an emulsification device experiences different stress levels and turbulence spectra at different positions. These differences compared to more idealized flow (i.e., to a homogenous and isotropic turbulence) could significantly alter the breakup process and mechanisms. Thus, there is a great need to investigate to what extent the insights gained from studying breakup in idealized conditions also applies to commonly used emulsification devices.

This study is part of a larger project attempting to understand turbulent drop breakup in emulsification devices. In a previous study, we developed a one-phase DNS model of a flow resembling the outlet chamber of a high-pressure homogenizer [41]. We have also developed a method for conducting numerical breakup experiments under conditions similar to those in a high-pressure homogenizer [26]. This previous investigation was, however, using the same assumption of homogenous and isotropic turbulence as in the majority of the other previous studies mentioned above. The specific aim of this contribution is to start exploring how much of the knowledge gained from the idealized isotropic configurations can be transferred to understanding the breakup process inside emulsification devices. This is achieved by combining the HPH DNS methodology and numerical drop breakup methodologies from our previous studies [26,41]. More specifically, this contribution aims to answer:

(i) how similar the breakup morphology is between the idealized case and the emulsification device for the same Weber number,
(ii) how similar the breakup times are, and
(iii) to what extent differences in the deformation process can be observed between the two configurations.

To reduce computational cost, the study is limited to a single Taylor-scale Reynolds number ($Re_\lambda = 54$). Moreover, the investigations are limited to cases where the interfacial tension is constant in space and time (as often assumed in similar studies), conditions like emulsifying a drop in the presence of an emulsifier with a high adsorption/desorption rate [27]. Nevertheless, this is a limitation since Marangoni effects could play a role in how the drop breakup proceeds, at least if we have emulsifiers that are either slow to adsorb or does not have a very high surface diffusivity [42-44].

2. Methodology

2.1. The two flow cases and DNS setup

Numerical breakup experiments are carried out in two different flow cases: an idealized fully periodic box with homogenous and isotropic (artificially injected) turbulence, henceforth referred to as 'case ISO', similar to the cases investigated in the majority of the previous studies [25-27,30,31,32], and the outlet chamber of a simplified HPH valve model [41], henceforth referred to as 'case HPH'.

The ISO case domain consists of a cubic box with length 2π and grid size 64^3. A periodic boundary condition is applied in all directions. A well-validated in-house DNS code is used to solve the Navier-Stokes equations ([45]; Crialesi-Esposito et al., 2021; [38,39]). The Arnold-Betrami-Childress forcing [46,47] is used to generate the homogeneous isotropic turbulence inside the domain. The computational domain of case ISO is presented in Fig. 1a.

The HPH case domain represents the scaled model of the outlet chamber of a simplified HPH valve [41]. The domain is depicted in Fig. 1b and the average flow field is illustrated in Fig. 2 (showing velocity magnitude averaged over time and across the spanwise y-dimension). The domain inlet (gap exit) is located on the lower-left of the domain (red face) with gap height $h = 750\ \mu m$, where the wall-adherent jet enters with a bulk velocity of $U_j = 16$ m/s. The green face on the right shows the outlet. The inlet boundary condition combines anisotropic synthetic velocity fluctuations with an average velocity profile obtained from experiments [41,48]. Periodic boundary conditions are applied in the spanwise y-direction and no-slip (stationary wall) boundary conditions are applied on all other boundaries, i.e. walls represented with dark grey color. A uniform Cartesian grid with a total of 173 million grid points constitutes the computational domain. More details can be found in the original one-phase DNS study [41].

To ensure a relevant comparison between the cases, the Taylor Reynolds number should be similar between the cases. For case HPH, however, Re_λ varies across the domain (due to the inhomogeneous flow). The value at the jet centerline, eight gap heights downstream of the gap exit ($Re_\lambda = 54$), is taken to be representative of case HPH (see blue marker in Fig. 1b). This is approximately the position where the drop starts to experience critical deformation, according to preliminary simulations. The fluid properties of case ISO are, therefore, set so as to also have $Re_\lambda = 54$.

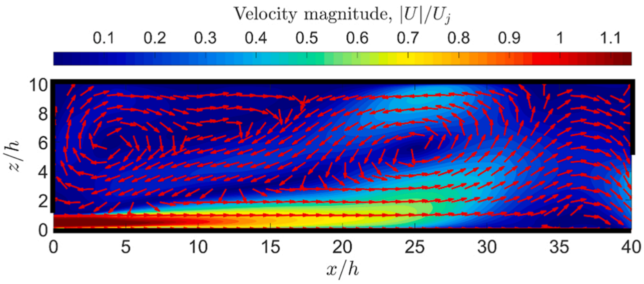

Fig. 2. Average velocity field for case HPH, reproduced from Olad et al. [49].

2.2. Numerical breakup experiments

The numerical experiments combine DNS, for describing the turbulent flow, with a highly-resolved volume-of-fluid (VOF) scheme–the Multi-dimensional tangent of hyperbola interface capturing method [50]–for describing the interface. Implementation details and extensive validations can be found in previous studies [38,39].

Each numerical experiment consists of injecting a single spherical drop into the flow-field. Care is taken to ensure that the turbulent flow has reached statistical convergence before the point of injection [26,41]. Due to the intermittent nature of turbulent flows, however, each drop experiences a different history of turbulent stresses. To investigate these variations, seven drops (labeled A, B, …G) are separately injected for each case and for each investigated Weber number. Each injection starts from a converged one-phase flow. Each drop is injected at a separate flow realization, differing from the previous injection point by no less than 80 Kolmogorov time-scales, τ_η.

Emulsification experiments typically suggest that the largest drop surviving passage is determined by three dimensionless numbers [26, 51] the Weber number,

$$We = \frac{2\rho_C \varepsilon^{2/3} D^{5/3}}{\gamma}, \tag{1}$$

the ratio between disperse and continuous phase viscosity, μ_D/μ_C, and the ratio between drop diameter and Kolmogorov length-scale, D/η. The viscosity ratio is kept constant at $\mu_D/\mu_C = 5$ and D_0/η is kept well above unity for all cases ($D_0/\eta = 38$ for case ISO and $D_0/\eta = 5$ for case HPH) ensuring turbulent inertial breakup [51].

Turbulent drop breakup in emulsification devices can typically be characterized by Weber numbers in the range 1–100 [26]. Previous investigations show characteristically different breakup morphologies across this range [26]. Consequently, three Weber numbers are studied in the present study: We = 1, We = 5 and We = 96. In an applied setting, We = 1 is comparable to what a drop just small enough to survive

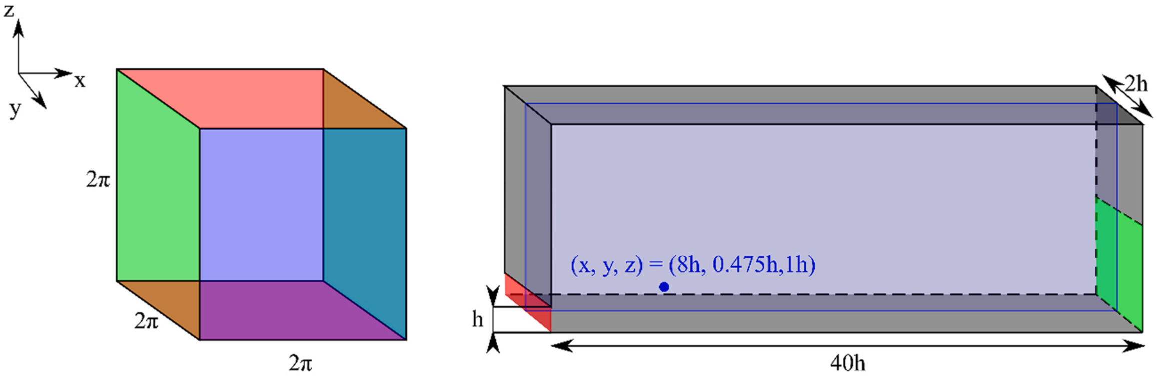

(a) (ISO)

(b) (HPH)

Fig. 1. The computational domains for cases ISO (a) and HPH (b). In b) the red area represents the inlet and the green the outflow boundary and the dimensions are expressed in h, where h = 750 μm. The blue plane shows the middle-plane in y-direction and the blue point in this plane shows the reference location for Taylor Reynolds number and the dissipation rate of TKE. (For interpretation of the references to colour in this figure legend, the reader is referred to the web version of this article.)

breakup experiences, We = 5 is comparable to what the smaller drops breaking in the device experience (i.e., breakup of the 'limiting drop') and We = 96 is comparable to what is experienced by the largest drops entering the device [26]. For case ISO, ε in Eq. 1 refers to the temporally and spatially averaged value across the domain and for case HPH, ε refers to the value at the reference location (jet centerline at $x/h = 8$), shown in Fig. 1b. Numerical experiments with these different Weber numbers are performed by varying the value of the interfacial tension [30], in order to ensure that the spatial resolution does not differ between the different cases.

For case ISO, a spherical $D_0 = 2$ drop is injected in the center of the domain, resulting in a spatial resolution of $D_0/\Delta x = 41$. In case HPH, a spherical $D_0 = h/3$ drop is injected slightly downstream of the gap exit in the center of the jet, $(x,y,z) = (0.8\,h, 0.5\,h, 1\,h)$–the $0.8\,h$ offset is used to ensure that the synthetic fluctuations generated at the inlet do not add artificial deformation to the drop. This results in a spatial resolution of $D_0/\Delta x = 20$ for case HPH. This lower resolution is necessary in order to limit the computational cost for case HPH (note that the number of computational cells is a factor 650 larger for case HPH compared to case ISO). The effect of this difference in resolution between cases on the breakup morphology and breakup characteristics are discussed in detail in Section 2.4. (Note that the ISO case simulations were carried out in dimensionless form, as typically the case under idealized conditions, whereas the HPH case simulations were carried out in the physical units.).

Each numerical simulation is run either until breakup is observed or until the drop has spent at least 100 τ_η (Kolmogorov times) in the turbulence (corresponding to the passage time through an emulsification device). Drops that do not reach a critically deformed state at this point, are expected to survive the passage.

2.3. First effective breakup

Drop breakup (especially when the initial drop diameter is relatively large) often goes through a sequence where the drop is first deformed and breaks into two or more fragments. Each of these large fragments might continue deforming and/or break into several sub-fragments [52]. The main interest in this study is this first stage of the breakup process, since this is what determines the limit in terms of the largest drop surviving passage (which in turn determines the physical stability of the emulsion). Therefore, a clear definition of the first phase of the breakup process is critical to enable clear comparisons.

Solsvik et al. [52] defined the state of 'initial breakup' when the first fragment detaches, and this has proven to be a useful concept in subsequent investigations. Preliminary simulations, however, show that small fragments are occasionally detached (due to external stress), after which the rest of the drop is able to relax and survive further breakup for a long time period. Although, these drops have technically undergone a breakup event, they are virtually unaffected from an applied perspective (the emulsion stability is only marginally affected if a fragment containing less than a small percentage of the drop volume is detached). In the present study, the term 'first effective breakup' is therefore used to define the first detachment of a fragment with more than 2 % of the initial drop volume.

An example can be seen in Fig. 3, showing the drop morphology for one of the simulated cases at eight different points in time. The first (small) fragment detaches at $t/\tau_\eta = 26.0$ ('initial breakup', grey arrow). This fragment, however, quickly re-coalesces with the larger fragment, after which the drop relaxes. The first occurrence of a breakup event detaching a substantial drop volume appears considerably later at $t/\tau_\eta = 44.6$ ('first effective breakup', green arrow).

2.4. Grid independence

As discussed above, the HPH numerical breakup experiments were conducted with a lower spatial resolution than for the ISO case. This was deemed necessary to limit the computational cost of the HPH case which has a considerably larger domain size. The spatial resolution for the HPH is still high in relation to the Kolmogorov length-scale [41], implying that spatial resolution has no effect on the representation of the single-phase turbulent flow. However, the interface is less well-resolved in the HPH than in the ISO ($D_0/\Delta x = 20$ compared to $D_0/\Delta x = 41$).

To ensure that this does not influence the results, a grid independence study is carried out based on the ISO case: Using a previously suggested method [26,30], a spherical drop is injected into the converged one-phase turbulent flow of case ISO. The drop is either injected directly into the flow-field (resulting in $D_0/\Delta x = 41$) or into a field that has been interpolated to obtain half the initial resolution (resulting in $D_0/\Delta x = 20$). Turbulent forcing is turned off at the time of injection (cf. [30]). Injections are carried out for four drops (I, II, III and IV), one in each flow realization (separated by no less than 100 τ_η).

Of the four investigated flow realizations, two resulted in breakup (I and II) and two resulted in drops deforming but then relaxing back to spherical shape (III and IV). Fig. 4 shows the drop morphology at the

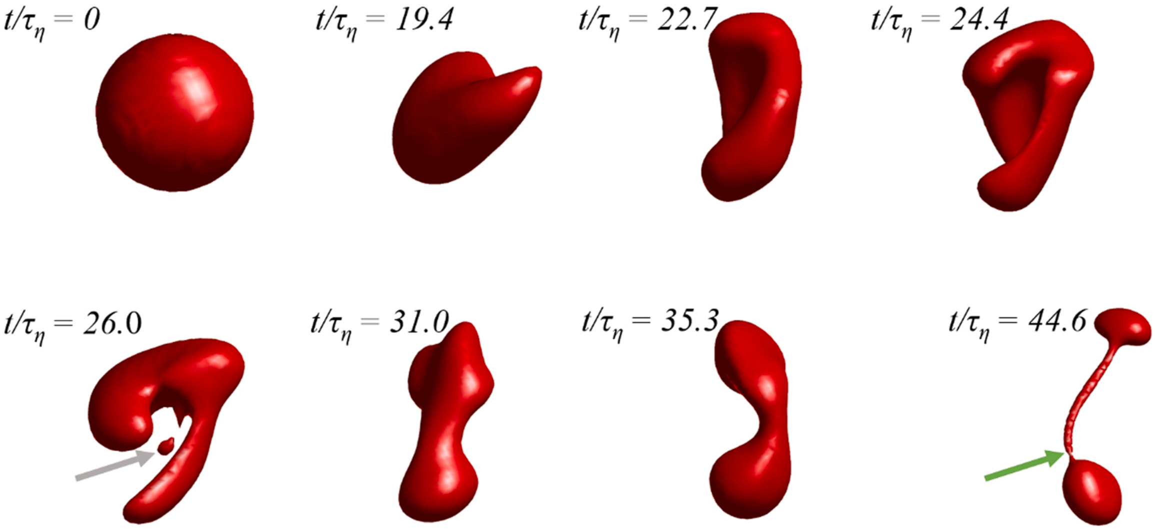

Fig. 3. Example sequence showing the drop morphology at eight different points in time, illustrating a minor fragment detaching at $t/\tau_\eta = 26.0$ ('initial breakup', grey arrow), but the first fragment of considerable volume detaching at $t/\tau_\eta = 44.6$ ('first effective breakup', green arrow). (Case HPH, We = 5, Drop C). (For interpretation of the references to colour in this figure legend, the reader is referred to the web version of this article.)

state of first effective breakup (iso-surfaces at VOF = 0.5) for the two drops that do break (I and II), comparing the coarser (left) and finer (right) mesh resolutions. (For both cases, first effective breakup coincides with initial breakup). The drops appear rougher with the coarser mesh. However, the simulations predict similar general morphology at the state of first effective breakup regardless of which mesh resolution is used. Using the coarser mesh results in an error of 3–6 % in the determination of the initial breakup time. The error in the global deformation extent (total interfacial area divided by the initial interfacial area of the unreformed drop, A/A_0) at initial breakup is even smaller (1–2 %), when comparing the coarser to the finer mesh.

Fig. 5 compares the drops that do not break, showing their morphologies at the time of maximum global deformation (i.e., maximum interfacial area), for the coarser (left) and finer (right) mesh. As above, morphological differences are small. The main difference is a slightly rougher appearance for the drop on the coarser mesh. Note, however, that for one of the cases (IV), the high curvature in the lower left corner makes it challenging for the iso-surfaces to display the interface, resulting in a small isolated high-VOF region. This should not, however, be misinterpreted as a detachment (as seen, this artificial fragment in Fig. 5 is substantially smaller than the initial breakup fragment in Fig. 3). Using the coarser mesh results in an error of 9–10 % when determining the time of maximum global deformation and an error of 0.2–2 % in the determination of the global deformation extent.

In summary, the simulations predict similar breakup morphologies and breakup behavior on the coarser and the finer mesh. The main difference is the less smooth appearance of the drops with the coarser mesh, an increased uncertainty in the breakup time (3–10 %) and total drop interfacial area (0.2–2 %), and the risk of small artificial fragments. The latter finding is an additional reason to focus comparisons on the first effective breakup rather than initial breakup (see Section 2.3). In summary, the difference in mesh resolution between the two cases is not expected to influence the conclusions of the present study.

3. Results and discussion

This section is organized as follows: Section 3.1 discusses the morphology at the first effective breakup and the deformation process leading to it. This section is divided in three parts, each focusing on one Weber number, comparing the two configurations under investigation (ISO vs HPH). The breakup time and its relation to the Weber number is discussed in Section 3.2 and Section 3.3, finally, investigates breakup position in the HPH, and discusses its relation to the inhomogeneous turbulent flow field.

3.1. Deformation and breakup morphology

3.1.1. We = 96 (corresponding to the largest drops entering the device)

Figs. 6–7 illustrate the shape of the drop at the instance of first effective breakup for the ISO and HPH cases, respectively (iso-surfaces of VOF = 0.5). Regardless of the flow realization (A, B, …G) and the flow case (ISO or HPH), the drop breaks after having been intensely deformed in multiple directions. This deformation pulls the drop into a thin sheet which eventually ruptures into a number of thin threads. Small fragments start detaching from this highly deformed structure, either in its sheet state or as these threads start to break (see Figs. 6–7). Note that several such small fragments have already been formed when reaching the state of first effective breakup in Figs. 6–7 (i.e., when the first fragment with a volume exceeding 2 % of the initial volume is detached). The finding of a strong and multi-directional deformation at high Weber numbers agrees well with results from previous investigations in homogenous and isotropic turbulence (Komrakova et al., 2019; [26]). Moreover, no clear difference is observed for the cases of ISO and HPH, indicating that this behavior at high Weber numbers generalizes to the more complex flow in the emulsification device.

Fig. 8 provides a further illustration of the deformation process for the different drops and flow cases, showing the total interfacial area (normalized by the surface area of the initial spherical drop) as a function of time (normalized by the Kolmogorov time-scale). A larger interfacial area corresponds to a (globally) more deformed drop. The deformation of the drops in case ISO (Fig. 8a) starts at the same time as the drops are injected into the turbulence. It continues monotonically until reaching the state of first effective breakup (disc markers). The drops injected in the HPH, however, are virtually un-deformed for the first 7.5–10 τ_η. This time corresponds to a streamwise position of x/h= 4–6, which is approximately at the point where the jet shear layers

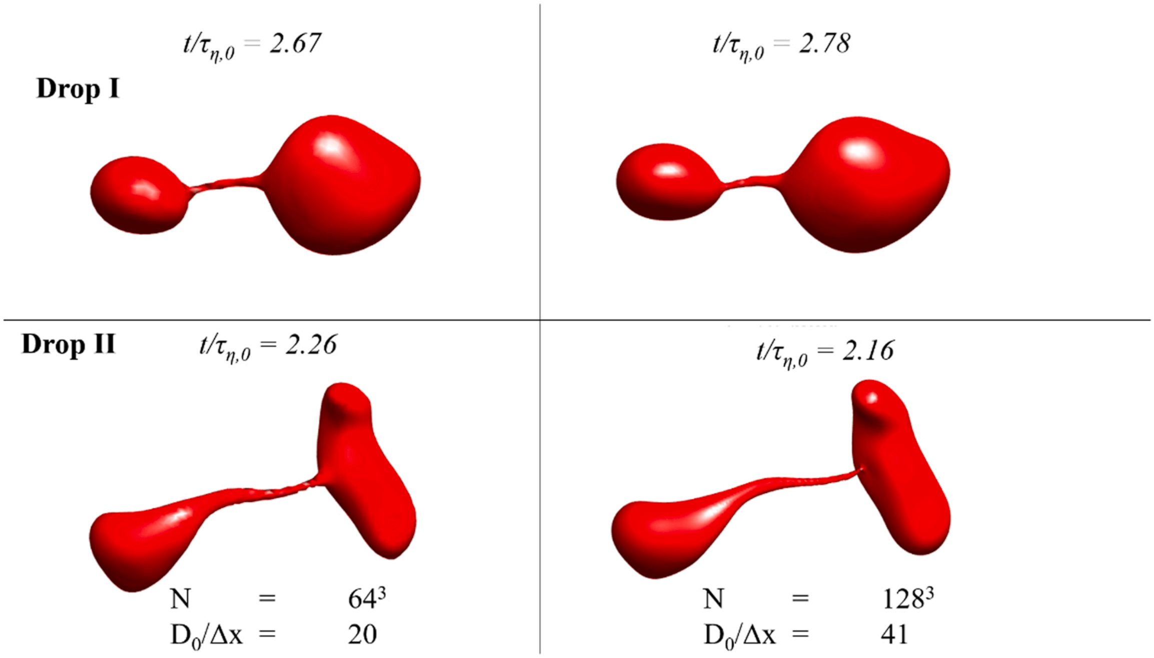

Fig. 4. Comparison of the grid resolution impact on the initial drop breakup morphology, showing drop I (upper row) and drop II (lower row). Left) Coarser grid (with the same resolution as that of case HPH). Right) finer grid (with the same resolution as that of case ISO).

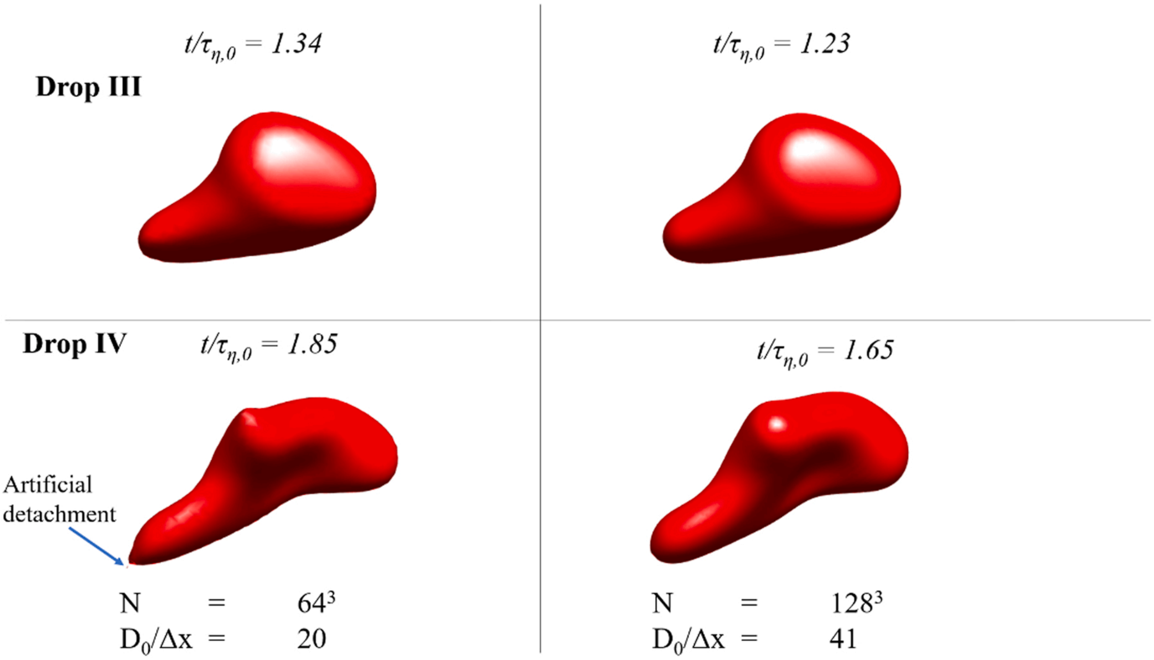

Fig. 5. Comparison of the grid resolution impact on the morphology of highest global deformation, showing drop III (upper row) and drop IV (lower row). Left) Coarser grid (with the same resolution as that of case HPH). Right) finer grid (with the same resolution as that of case ISO).

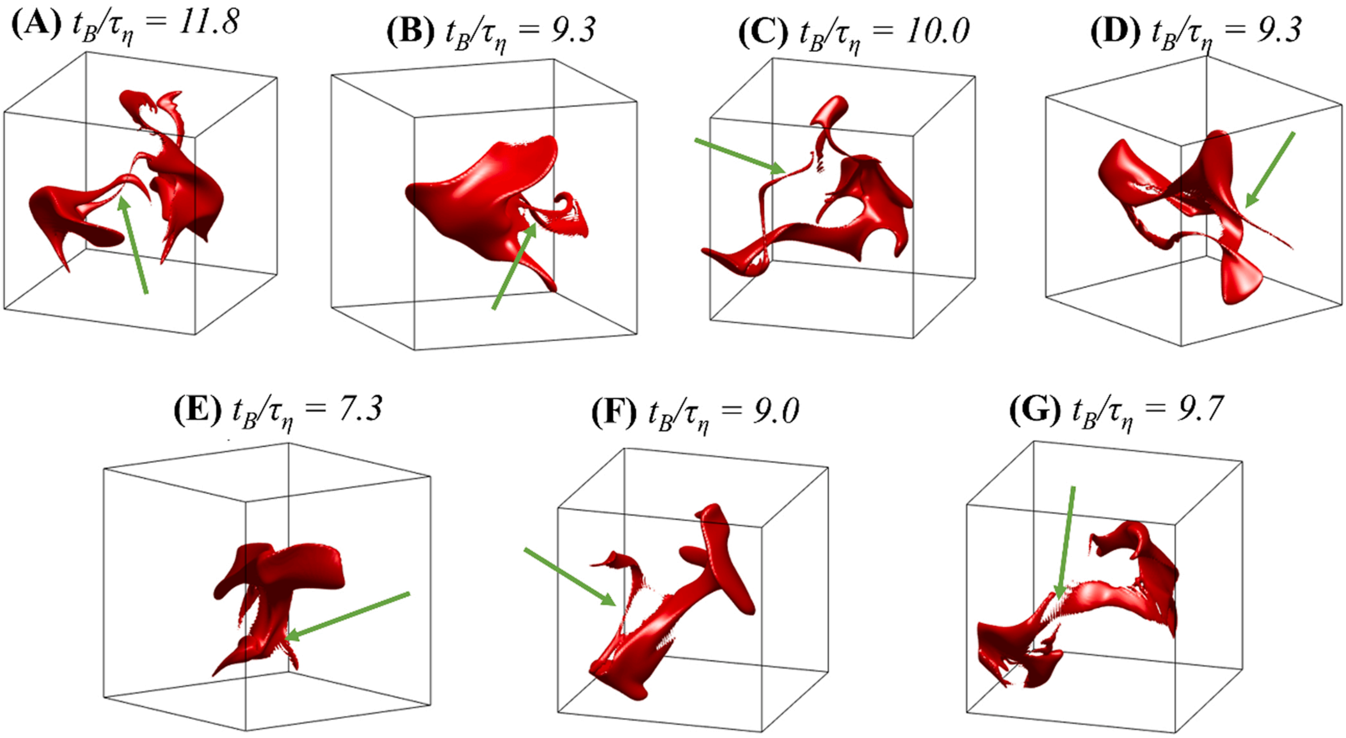

Fig. 6. Deformation morphology of drops for case ISO at the instance of first effective breakup showing drops A-G at We= 96. (Iso-surfaces of VOF=0.5). The first effective breakup time normalized with the Kolmogorov time-scale is specified for each case. Green arrows show the position of first effective breakup. The box displays the size of the simulation domain. (For interpretation of the references to colour in this figure legend, the reader is referred to the web version of this article.)

first have substantial levels of TKE [41], cf. Fig. 2. After this point, a majority of the drops show monotonically increasing deformations until reaching the state of first effective breakup.

3.1.2. *We = 5 (corresponding to a limiting drop entering the device)*

Figs. 9–10 illustrate the shape of the drop at the state of first effective breakup for the case with We = 5, for the ISO and HPH cases respectively (iso-surfaces at VOF = 0.5). Looking first at the case of homogenous and isotropic turbulence (case ISO) (Fig. 9), the drops deform and stretch, until a neck is formed with two bulbs of disperse phase on each side of it. The first effective breakup occurs at the neck (green arrows in Fig. 9). For all seven cases, the first initial breakup also coincides with

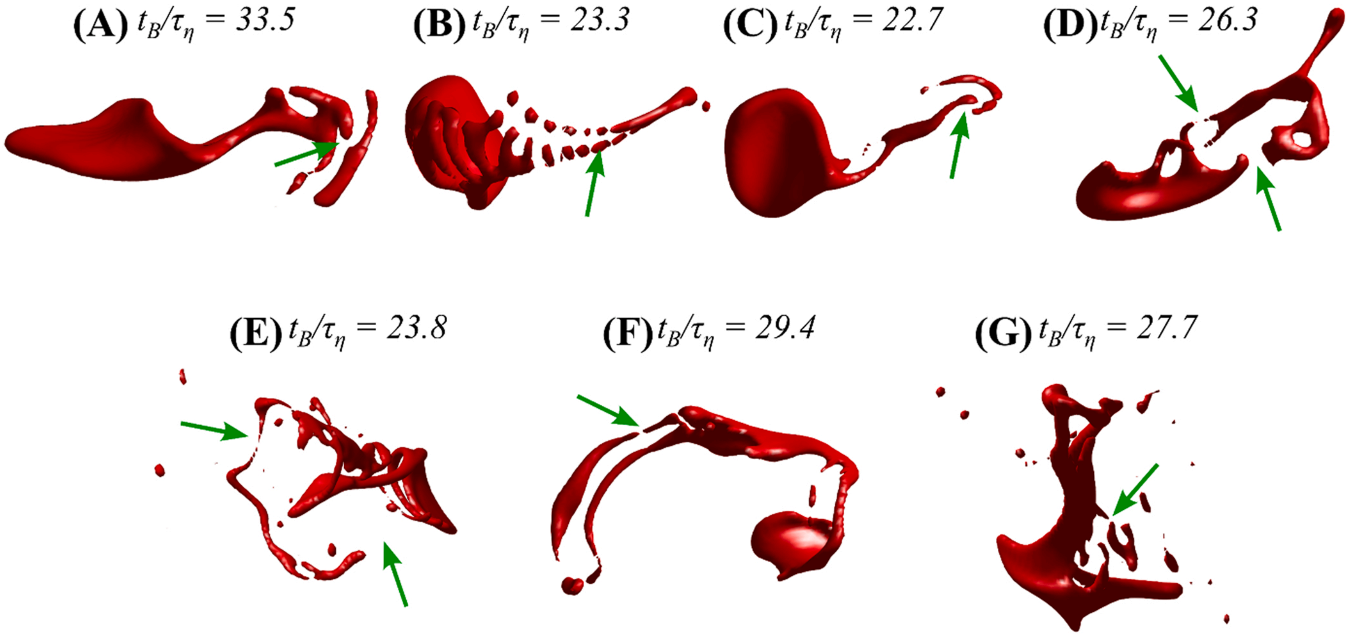

Fig. 7. Deformation morphology of drops for case HPH at the instance of first effective breakup showing drops A-G at We= 96. (Iso-surfaces of VOF=0.5). The first effective breakup time normalized with the Kolmogorov time-scale is specified for each case. Green arrows show the position of first effective breakup. (For interpretation of the references to colour in this figure legend, the reader is referred to the web version of this article.)

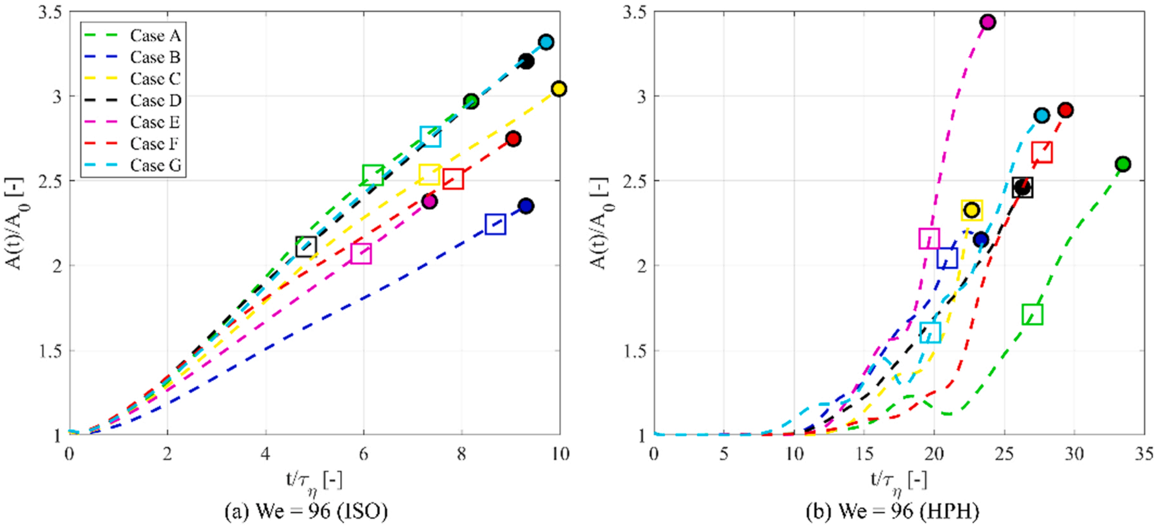

(a) We = 96 (ISO)

(b) We = 96 (HPH)

Fig. 8. Total interfacial area, A, as a function of time, t, for the cases of ISO (a) and HPH (b) at We= 96. Hollow squares mark the state of initial breakup and solid discs mark the state of first effective breakup.

the initial breakup (i.e., no detachment of < 2 % fragments are observed before the states in Fig. 9). This breakup behavior is well-known from previous investigations at similar Weber numbers on idealized and forced turbulence [26,27] and is referred to as a ‘neck-bulb’ mechanism; deformation at the neck increases the local curvature and, thus, the Laplace pressure. When the Laplace pressure at the neck exceeds that in the smaller bulb, a net destabilizing internal flow will form, leading to the inevitable breakup of the drop [27].

The drops injected in the HPH flow show a similar morphology at the state of first effective breakup. The majority of the drops still break after being deformed into two clearly distinguishable bulbs separated by a neck (A, B, C, E and G in Fig. 10). However, the bulbs are often more heavily deformed than in the idealized flow. Moreover, in two of the cases (D and E in Fig. 10), the deformation has become sufficiently large to allow minor fragments to detach before reaching the state of first effective breakup. This suggests that the breakup processes in the emulsification device (case HPH) is similar to that in the idealized flow (case ISO), but not identical to it.

Further insights into the difference between the deformation processes can be gained from Fig. 11, showing the evolution of the drop interface over time for the two cases. Just as was seen for the higher We (cf. Fig. 8), drops injected in the homogenous and isotropic turbulence (case ISO) start deforming directly at injection, whereas deformation is delayed until $t/\tau_\eta = 7.5–10$ in the emulsification device (case HPH).

Compared to the higher Weber number (We = 96), deformation is not typically monotonic at We = 5. Some drops start deforming and then go into a brief period of relaxation after which deformation resumes. Fig. 11 shows how this behavior, previously reported for drops in homogenous and isotropic turbulence [26], can also be seen in the HPH (e.g., case B and D).

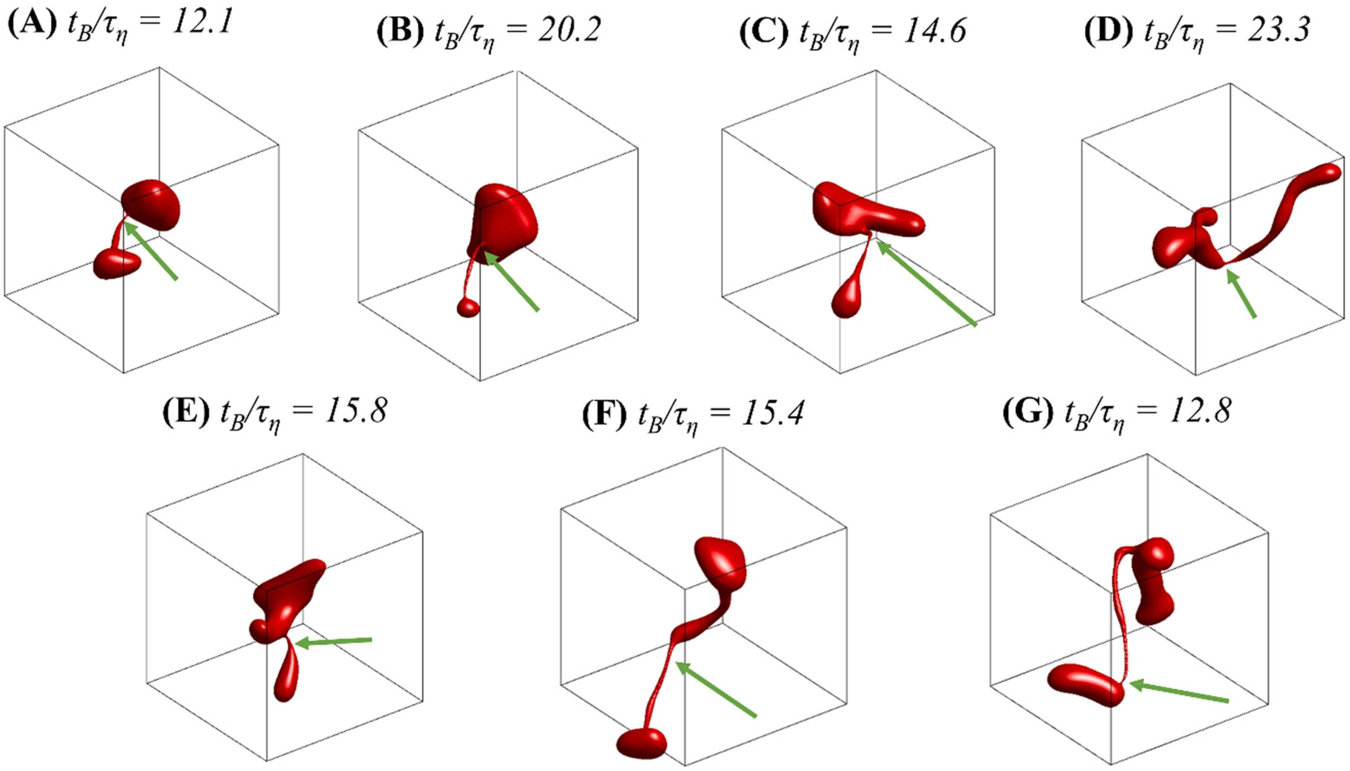

Fig. 9. Deformation morphology of drops for case ISO at the instance of first effective breakup showing drops A-G at We= 5 (Iso-surfaces of VOF=0.5). The first effective breakup time normalized with the Kolmogorov time-scale is specified for each case. Green arrows show the position of first effective breakup. The box displays the size of the simulation domain. (For interpretation of the references to colour in this figure legend, the reader is referred to the web version of this article.)

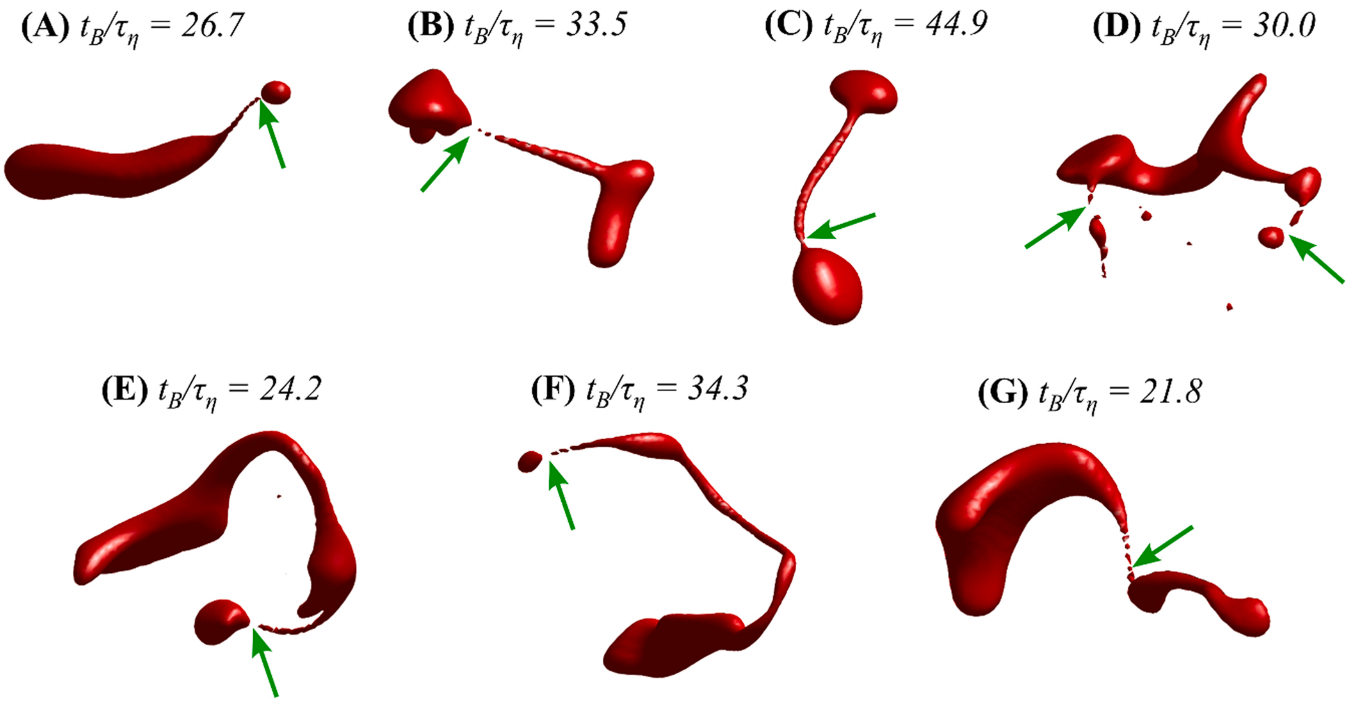

Fig. 10. Deformation morphology of drops for case HPH at the instance of first effective breakup showing drops A-G at We= 5. (Iso-surfaces of VOF=0.5). The first effective breakup time normalized with the Kolmogorov time-scale is specified for each case. Green arrows show the position of first effective breakup. (For interpretation of the references to colour in this figure legend, the reader is referred to the web version of this article.)

3.1.3. We = 1 (corresponding to the smallest drops entering the device)

Figs. 12 and 13 show the final snapshot of drop morphology, for the ISO and HPH cases respectively, for the numerical experiments conducted at We = 1. None of the drops injected in the homogeneous and isotropic turbulence (case ISO) at this Weber number are fragmented. As seen in Fig. 12, all drops are in a relaxed, nearly spherical

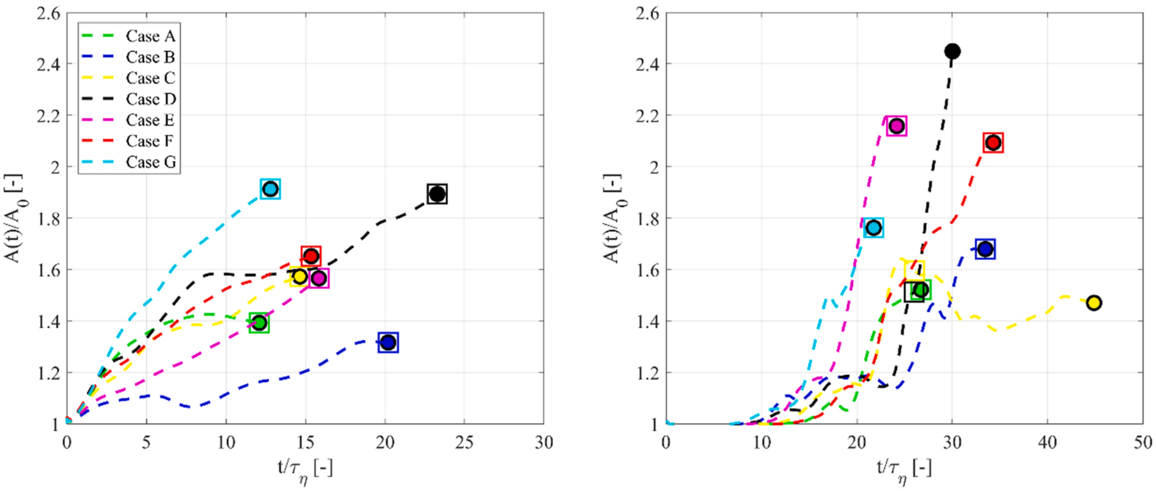

(a) We = 5 (ISO)   (b) We = 5 (HPH)

Fig. 11. Total interfacial area, A, as a function of time, t, for the cases of ISO (a) and HPH (b) at We= 5. Hollow squares mark the state of initial breakup and solid discs mark the state of first effective breakup.

shape at $t = 100\ \tau_\eta$ (i.e., at the time drops typically exit the emulsification device). This also applies for the majority of drops injected in the emulsification device (case HPH). Only one drop in case HPH (drop E in Fig. 13) breaks up at this Weber number. (For a discussion on differences in breakup behavior between drops/flow-realizations, see Section 3.3).

Fig. 14 displays the extent of global deformation as a function of time for the two configurations and the seven different drops with We = 1, where we can observe a different behavior for ISO and HPH. For drops experiencing the homogenous and isotropic turbulence (case ISO), the total surface area shows an oscillatory behavior, with a sequence of deformations and relaxations. The amplitude of the deformation shows a steady increase over time, although the slope is relatively small, so that the drops still appear approximately spherical at $t = 100\ \tau_\eta$ (Fig. 12). This oscillatory behavior, with an amplitude growing over time, is similar to what Risso and Fabre [19] refers to as a resonance deformation mechanism and has previously been described mathematically by the Rayleigh-Lamb model [19,53] in which the drop interface oscillates (deforms and relaxes) with a characteristic frequency f_2 and a dampening rate β_2 [12,19,54]. Using the disperse and continuous phase properties used in the numerical experiments, and the analytical method suggested by Miller and Scriven [55], the theoretical characteristic oscillation was estimated to be 9 τ_η. This agrees fairly well with the observed oscillation period in Fig. 14a, which is approximately in the range 1–10 τ_η. This suggests that the Rayleigh-Lamb model provides a

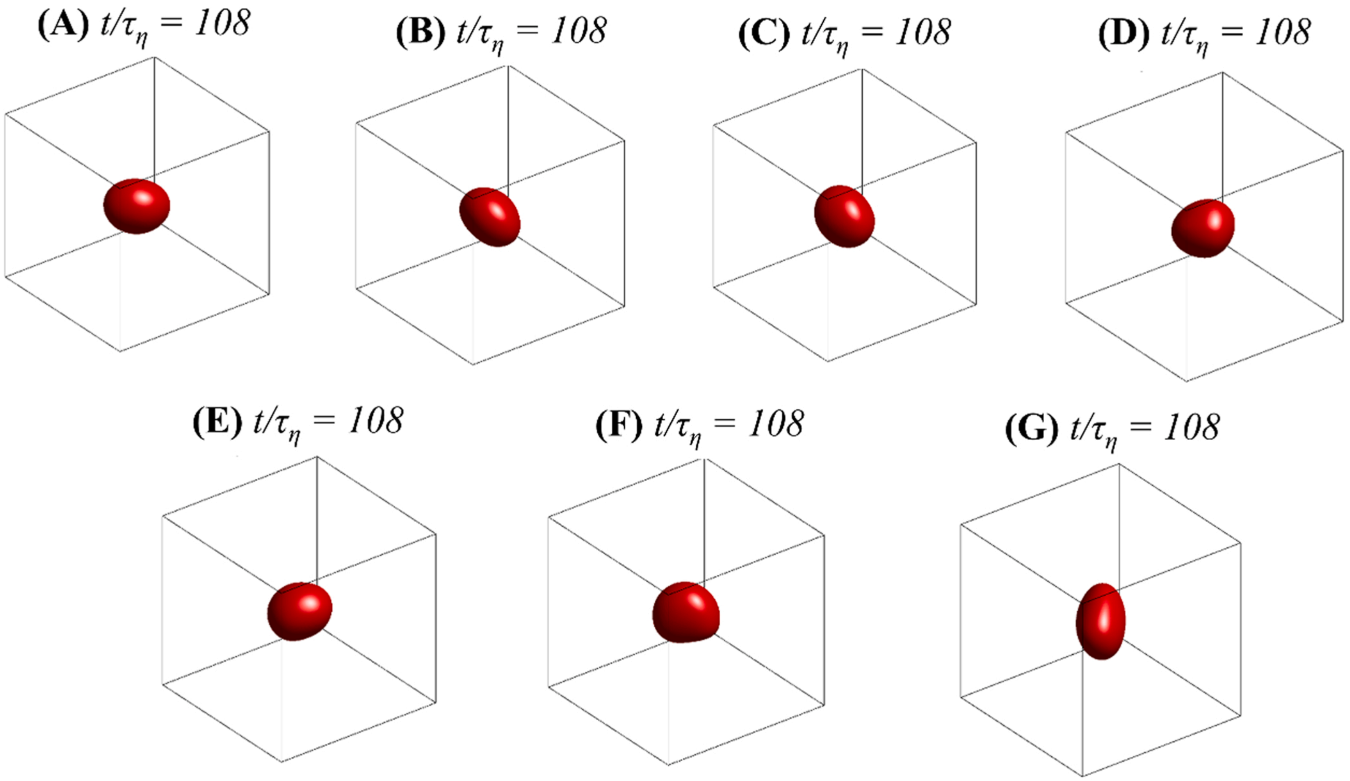

Fig. 12. Deformation morphology of drops for case ISO at the instance of first effective breakup showing drops A-G at We= 1. (Iso-surfaces of VOF=0.5). The final simulation times normalized with the Kolmogorov time-scale are specified for each case. The box displays the size of the simulation domain.

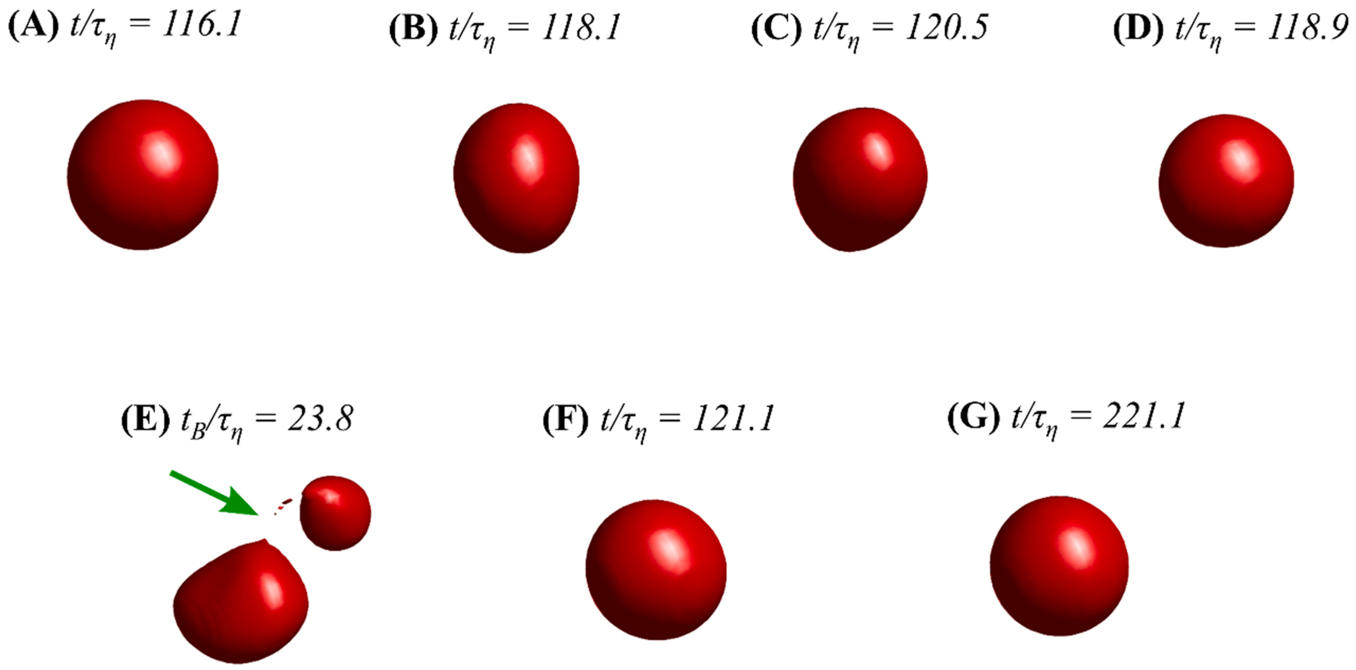

Fig. 13. Deformation morphology of drops for case HPH at the instance of first effective breakup showing drops A-G at We= 1. (Iso-surfaces of VOF=0.5). The final simulation times normalized with the Kolmogorov timescale are specified for each case. For case E where breakup occurs, the normalized first effective breakup time is specified. Green arrow shows the position of first effective breakup. (For interpretation of the references to colour in this figure legend, the reader is referred to the web version of this article.)

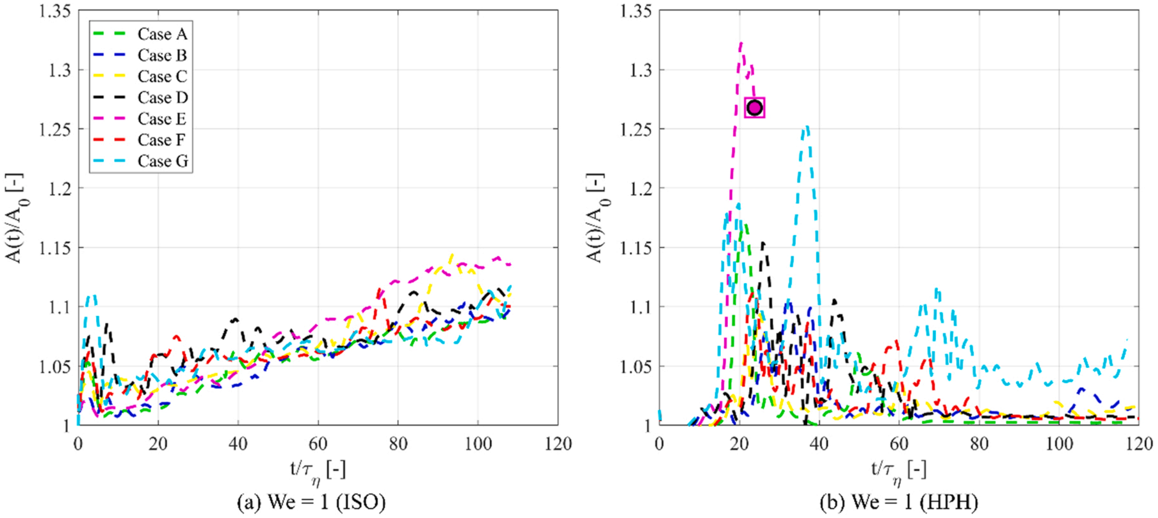

(a) We = 1 (ISO)

(b) We = 1 (HPH)

Fig. 14. Total interfacial area, A, as a function of time, t, for the cases of ISO (a) and HPH (b) at We= 1. Hollow square marks the state of initial breakup and solid disc marks the state of first effective breakup.

fairly good description of the drop in the idealized flow (case ISO).

As seen in Fig. 14b, the deformation progresses differently for the drops experiencing the inhomogeneous and anisotropic turbulence of case HPH. As for drops with higher Weber numbers, they start deforming only after reaching positions of high turbulence levels. Drops are deformed and typically pass through a few deformation-relaxation cycles, but without showing an increase in oscillation amplitude (Fig. 14b). Also note that the first deformation cycle has a substantially higher amplitude than for case ISO. However, with the exception of drop E (where the initial deformation is sufficient to lead to breakup), the drops exit the HPH in a less deformed state than for case ISO.

The differences in the deformation process are expected because of the inhomogeneity in the emulsification device. A drop injected in case HPH experiences high stress levels when passing the shear layers (see Fig. 2) but leaves this region relatively quickly, after which turbulent stresses decrease to low levels. Thus, although the same physics applies to the different cases, drops in the emulsification device do not experience high stress for a sufficiently long period of time to excite the resonance mechanism.

3.2. Breakup time

A summary of the time of first effective breakup (t_B) and initial breakup (t_{IB}), comparing the different Weber numbers and drop realizations, can be found in Tables 1–2. Table 1 displays the data for case ISO and Table 2 for case HPH.

As observed in Table 1, the breakup time decreases when increasing the Weber number for the drops experiencing homogenous and isotropic turbulence. This applies for the average as well as when comparing across drops of different We injected in the same flow realization (i.e., comparing across rows), and is expected because drops experiencing a higher deforming stress should break earlier [56].

For the drops in the emulsification device (case HPH), the situation is more complex. Statistically, there is no significant decrease in breakup time (neither when defined as the time of initial breakup nor when defined as first effective breakup) with increasing Weber number. Looking at the individual flow realizations, there is also a drop (G) that experiences its first effective breakup slightly earlier at We = 5 than at We = 96. As for the difference in the global deformation evolution (Figs. 8, 11 and 14), this can be explained by the inhomogeneity of the turbulent flow in the emulsification device (case HPH), and shows that it is difficult to apply breakup time correlations developed for idealized conditions (e.g., [56]) to predict breakup in the emulsification device.

3.3. Breakup position

As discussed in Section 3.2, the time at which the drop enters a region of highly intense turbulence (created in the outer jet shear layer) appears to be a better breakup predictor than the time spent in the flow for the case HPH. Thus, a more detailed understanding of how breakup relates to the drop trajectories is of interest.

Fig. 15 illustrates the trajectories for the different drops and Weber numbers under investigation. Squares mark the initial breakup and discs the first effective breakup (see definitions in Section 2.3). The contour of the time-averaged dissipation rate of TKE (as obtained from the one-phase DNS and averaged in the spanwise y-direction, see [41]), can be seen in the background. As shown in the figure, a highly dissipative region exists at a distance $x/h = 4–10$ downstream of the gap exit (i.e., from the domain inlet) (a more comprehensive discussion of the one-phase turbulent field can be found in [41]). Breakup is observed inside or shortly downstream of this region at $x/h = 9–18$. This observation is also consistent with experimental investigations on similar systems [6–9].

As expected, each drop will follow its own trajectory that differs somewhat from the other drops injected in the same conditions due to the stochastic nature of the turbulence. The results in Fig. 15 imply that the drop trajectory has an impact on the breakup time, which is observed most prominently for the drops with We = 5. The drops which travel closer to the highly dissipative shear layer (drop G, E and D in Fig. 15b) break earlier. Drops passing further from the shear layers, closer to the center of the jet (drops A and C in Fig. 15b), survive longer. We can also see that the drop venturing the furthest into the dissipative region (G in Fig. 15b) is also the first to break. This can be seen more clearly in Fig. 16, displaying the time-average dissipation rate of TKE at the location of the drop centroid (spatially averaged across a sphere with diameter 2 D_0) as a function of time.

However, Figs. 15–16 also show that drop trajectories and average flow fields are unable to predict all of the observed differences in breakup behavior. At We = 1, for example, drops G and E follow approximately the same trajectory through the domain (see Fig. 15a), consequently, they also visit locations with approximately the same time-averaged dissipation rate of TKE (see Fig. 16a). However, drop E breaks, whereas drop G only reaches a modest degree of global deformation, $A/A_0 = 1.2$, at this position (see Fig. 14b). Drop G is able to relax further downstream and exits the device intact. This is not unexpected in the light of previous investigations. Already in an idealized homogenous and isotropic turbulence, the details of how turbulent structures interact with, deform and eventually break a drop is complex. Intermittency leads to substantial differences in the instantaneous turbulent stresses, so that very different turbulent stresses are measured at the same spatial location depending on when it is visited. Previous investigations on idealized flows also suggest that the breakup requires a sequence of several eddy-drop interactions [26], that eddies relatively far from the drop participate in deforming it [33] and that the orientation between turbulent eddies and drops plays an important role in determining the efficiency to critically break the drop [31]. There is yet no combined and generally accepted model able to deterministically predict what causes breakup for a single drop based on the surrounding turbulent field, even for the idealized case of homogenous and isotropic forced turbulence. Further investigations aiming to provide such an understanding are possible exploiting the data generated from the numerical experiments underlying this investigation, and will be performed later in the project.

Table 1
Time of initial breakup, t_{IB}, and time of first effective breakup, t_B, for the seven flow realizations for case ISO.

Drop	t_B/τ_η			t_{IB}/τ_η		
	We =1	We =5	We =96	We =1	We =5	We =96
A	>100	12.1	8.2	>100	12.1	6.2
B	>100	20.2	9.3	>100	20.2	8.7
C	>100	14.6	10.0	>100	14.6	7.3
D	>100	23.3	9.3	>100	23.3	4.8
E	>100	15.8	7.3	>100	15.8	5.9
F	>100	15.4	9.0	>100	15.4	7.8
G	>100	12.8	9.7	>100	12.8	7.4
Mean	>100	16.3	9.5	>100	16.3	6.9
Std.	NA	4.0	1.3	NA	4.0	1.3

Table 2
Time of initial breakup, t_{IB}, and time of first effective breakup, t_B, for the seven flow realizations for case HPH.

Drop	t_B/τ_η			t_{IB}/τ_η		
	We = 1	We = 5	We = 96	We = 1	We = 5	We = 96
A	>116	26.7	33.5	>116	26.7	26.7
B	>116	33.5	23.3	>116	33.5	21.3
C	>116	44.9	22.7	>116	26.0	22.7
D	>116	30.0	26.3	>116	26.0	26.3
E	23.8	24.2	23.8	23.8	24.2	19.3
F	>116	34.3	29.4	>116	34.3	29.4
G	>116	21.8	27.7	>116	21.8	19.7
Mean	NA	30.8	27.7	NA	27.5	23.6
Std.	NA	7.7	3.9	NA	4.7	3.9

4. Conclusions

The objective of this study was to identify similarities and dissimilarities between turbulent drop breakup obtained from interface-resolved simulations in homogenous and isotropic turbulence (case ISO) (as it has typically been studied previously) and in a model emulsification device (case HPH) (which is of great industrial interest). To summarize the main findings of this work:

- The breakup morphology is similar when comparing the two cases, with sheet-rupture breakup [26] at We = 96, neck-bulb breakup [27] at We = 5 and mainly deformation-relaxation oscillations [19] at We = 1. Differences are, however, also observed: i) the drop deformation is more multi-directional already at lower Weber numbers for case HPH (possibly due to the inhomogeneity of the flow). ii) One breakup event was recorded at We = 1 for case HPH, whereas none was recorded for case ISO. However, the total number of flow realizations is too low to draw definite conclusions on this.
- For case ISO, the breakup time decreases with the Weber number (as predicted theoretically, see e.g., [56]). For the HPH, however, the situation is more complex, due to the inhomogeneous turbulent field. Drops appear to deform and break relatively soon after entering the high turbulence intensity zone downstream of the gap exit, with no significant dependence on the Weber number. First effective breakup occurs in a region 9–18 gap heights downstream of the gap exit for

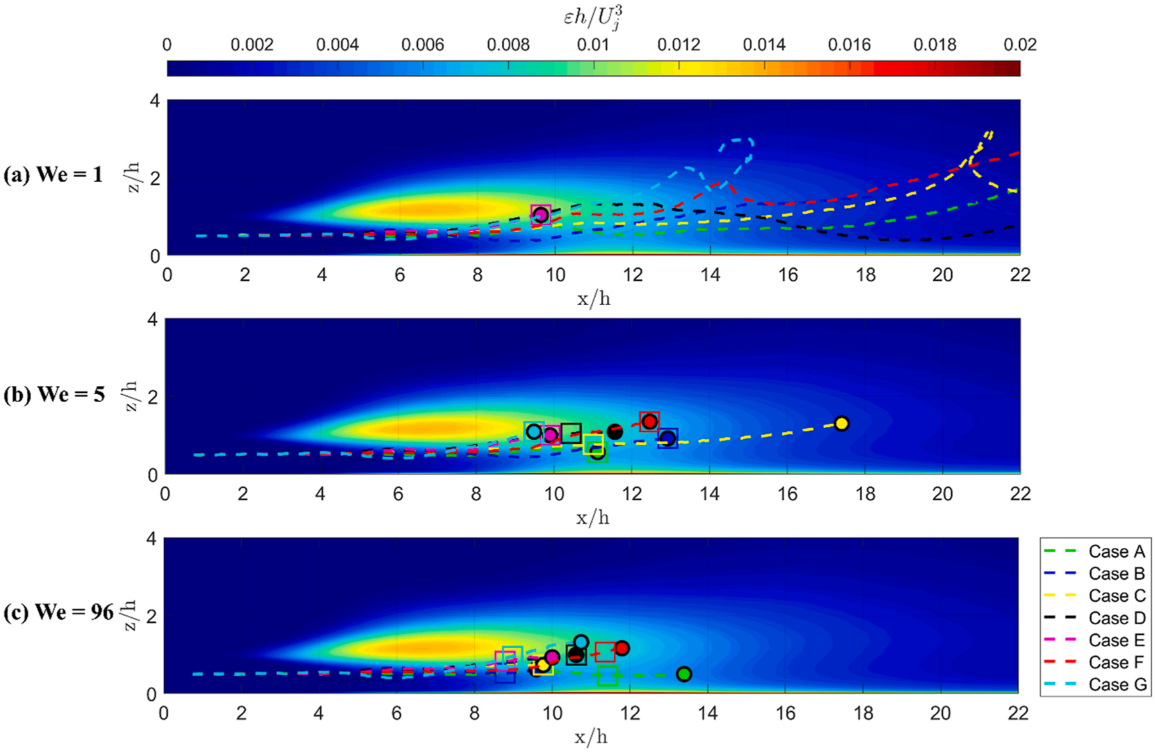

Fig. 15. Drop trajectories (dashed lines) with positions of initial breakup (hollow squares) and first effective breakup (solid discs) in the x-z plane of case HPH. Trajectories are showed on top of the normalized time-averaged dissipation rate of TKE contour (as obtained from the one-phase DNS, [41]). a) We = 1, b) We = 5, c) We = 96.

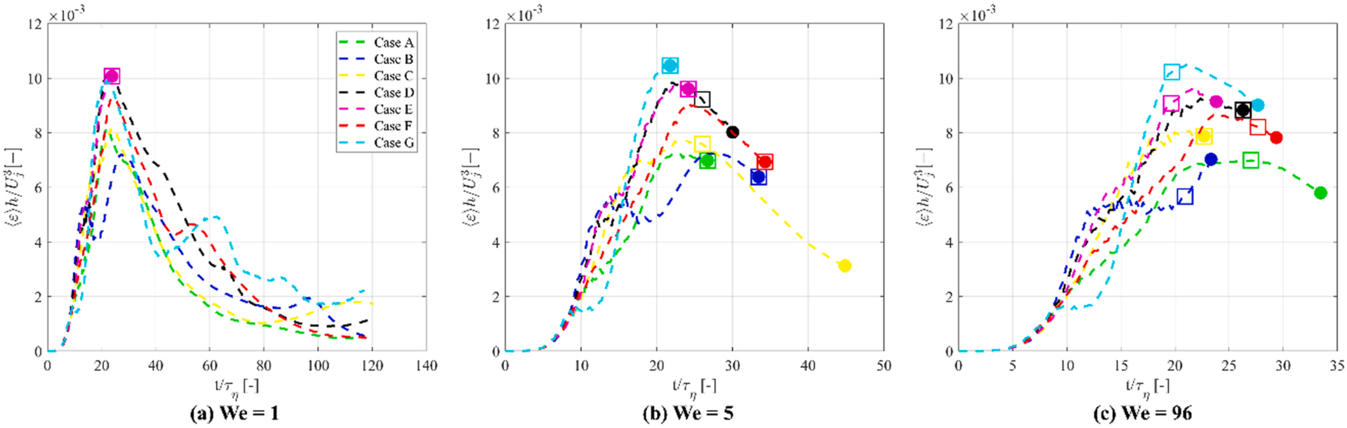

(a) We = 1

(b) We = 5

(c) We = 96

Fig. 16. Temporally- and spatially-averaged dissipation rate of TKE (averaged inside a sphere with diameter 2 D_0 and centered at the drop centroid) along the drop trajectories for case HPH. (a) We = 1, (b) We = 5, and (c) We = 96. Hollow squares mark the state of initial breakup and solid discs mark the state of first effective breakup.

the geometry considered here, with no significant effect of the Weber number (at least for the number of flow realizations currently available, i.e., 7 for each Weber number).

- Both similarities and differences can be seen in the deformation process. Regardless of the flow case, high Weber number typically gives rise to deformations continuously increasing with time, whereas cycles of deformations and relaxation are observed at low Weber number. For the emulsification device, the onset of the first deformation is delayed until the drop enters the highly dissipative region. Moreover, for the low Weber number, corresponding to the smallest drops entering the device (We = 1), the oscillation amplitude does not grow over time in the HPH as it does in the idealized flow (due to the decay of the turbulence intensity, forcing the deformation, further downstream).

Overall, these results suggest that the breakup mechanism as a function of Weber number is similar between the two configurations, with the inhomogeneity of the emulsification device introducing additional complexity in the breakup time and triggering a more multi-directional breakup. Since working with an idealized system is often substantially less costly from a computational perspective (650 fewer computational cells when comparing case ISO to case HPH in the present study), a combination of approaches (identifying phenomena and mechanisms using homogeneous and isotropic turbulence, and validating/identifying non-idealities using specific emulsification device geometry) is a promising route for further investigations into the nature of turbulent drop breakup in industrially relevant emulsifications.

CRediT authorship contribution statement

Peyman Olad: Writing – original draft, Conceptualization, Formal analysis, Investigation, Visualization. **Fredrik Innings**: Supervision, Conceptualization (Prof Innings passed away before the manuscript could be submitted). **Marco Crialesi-Esposito:** Supervision, Methodology, Software. **Luca Brandt**: Writing – review & editing, Supervision, Methodology, Software. **Andreas Håkansson**: Writing – review & editing, Supervision, Conceptualization, Resources, Funding acquisition, Visualization.

Declaration of Competing Interest

The authors declare that they have no known competing financial interests or personal relationships that could have appeared to influence the work reported in this paper.

Data availability

Data will be made available on request.

Acknowledgements

This research was funded by The Swedish Research Council (VR), grant number 2018-03820, and Tetra Pak Processing Systems AB.

References

[1] D.J. McClements. Food Emulsions: Principles, Practices, and Techniques, third ed., CRC Press, 2015 https://doi.org/10.1201/b18868.

[2] M. Rayner, P. Dejmek. Engineering Aspects of Food Emulsification and Homogenization, first ed., CRC Press, 2015 https://doi.org/10.1201/b18436.

[3] A. Håkansson, Emulsion formation by homogenization: current understanding and future perspectives, Annu. Rev. Food Sci. Technol. 10 (2019) 239–258, https://doi.org/10.1146/annurev-food-032818-121501.

[5] A. Håkansson, H.H. Mortensen, R. Andersson, F. Innings, Experimental investigations of turbulent fragmenting stresses in a rotor-stator mixer. Part 1. Estimation of turbulent stresses and comparison to breakup visualizations, Chem. Eng. Sci. 171 (2017) 625–637, https://doi.org/10.1016/j.ces.2017.06.042.

[4] M. Ashar, D. Arlov, F. Carlsson, F. Innings, R. Andersson, Single droplet breakup in a rotor-stator mixer, Chem. Eng. Sci. 181 (2018) 186–198, https://doi.org/10.1016/j.ces.2018.02.021.

[6] F. Innings, C. Trägårdh, Visualization of the drop deformation and break-up process in a high-pressure homogenizer, Chem. Eng. Technol. 28 (2005) 882–891, https://doi.org/10.1002/ceat.200500080.

[7] F. Innings, L. Fuchs, C. Trägårdh, Theoretical and experimental analyses of drop deformation and break-up in a scale model of a high-pressure homogenizer, J. Food Eng. 103 (2011) 21–28, https://doi.org/10.1016/j.jfoodeng.2010.09.016.

[8] K. Kelemen, S. Gepperth, R. Koch, H.J. Bauer, H.P. Schuchmann, On the visualization of droplet deformation and breakup during high-pressure homogenization, Microfluid. Nanofluidics 19 (2015) 1139–1158, https://doi.org/10.1007/s10404-015-1631-z.

[9] B. Mutsch, F.J. Preiss, T. Dagenbach, H.P. Karbstein, C.J. Kähler, Scaling of droplet breakup in high-pressure homogenizer orifices. Part II: visualization of the turbulent droplet breakup, ChemEngineering 5 (2021), e5010007, https://doi.org/10.3390/chemengineering5010007.

[10] A. Håkansson, An experimental investigation of the probability distribution of turbulent fragmenting stresses in a high-pressure homogenizer, Chem. Eng. Sci. 177 (2018) 139–150, https://doi.org/10.1016/j.ces.2017.11.045.

[11] R. Andersson, B. Andersson, On the breakup of fluid particles in turbulent flows, AIChE J. 52 (6) (2006) 2020–2030, https://doi.org/10.1002/aic.10831.

[12] S. Galinat, L. Garrido Torres, O. Masbernat, Breakup of a drop in a liquid-liquid pipe flow through an orifice, AIChE J. 53 (2007) 56–68, https://doi.org/10.1002/aic.11055.

[13] E.H. Herø, N. La Forgia, J. Solsvik, H.A. Jakobsen, Single drop breakage in turbulent flow: statistical data analysis, Chem. Eng. Sci. X 8 (2020), e100082, https://doi.org/10.1016/j.cesx.2020.100082.

[14] N. La Forgia, E.H. Herø, H.A. Jakobsen, High-speed image processing of fluid particle breakage in turbulent flow, Chem. Eng. X 12 (2021), e100117, https://doi.org/10.1016/j.cesx.2021.100117.

[15] S. Maaß, M. Kraume, Determination of breakage rates using single drop experiments, Chem. Eng. Sci. 70 (2012) 146–164, https://doi.org/10.1016/j.ces.2011.08.027.

[16] A.U.M. Masuk, A.K.R. Salibindla, R. Ni, Simultaneous measurements of deforming Hinze-scale bubbles with surrounding turbulence, J. Fluid Mech. 910 (2021) A21, https://doi.org/10.1017/jfm.2020.933.

[17] S. Nachtigall, D. Zedel, M. Kraume, Analysis of drop deformation dynamics in turbulent flow, Chin. J. Chem. Eng. 24 (2) (2016) 264–277, https://doi.org/10.1016/j.cjche.2015.06.003.

[18] Y. Qi, S. Tan, N. Corbitt, C. Urbanik, A.K.R. Salibindla, R. Ni, Fragmentation in turbulence by small eddies, Nat. Commun. 13 (2022) 469, https://doi.org/10.1038/s41467-022-28092-3.

[19] F. Risso, J. Fabre, Oscillations and breakup of a bubble immersed in a turbulent field, J. Fluid Mech. 372 (1998) 323–355, https://doi.org/10.1017/S0022112098002705.

[20] J. Solsvik, H.A. Jakobsen, Single drop breakup experiments in stirred liquid–liquid tank, Chem. Eng. Sci. 131 (2015) 219–234, https://doi.org/10.1016/j.ces.2015.03.059.

[21] J. Vejražka, M. Zedníková, P. Stranovský, Experiments on breakup of bubbles in a turbulent flow, AIChE J. 64 (2018) 740–757, https://doi.org/10.1002/aic.15935.

[22] S. Elghobashi, Direct numerical simulation of turbulent flows laden with droplets or bubbles, Annu. Rev. Fluid Mech. 51 (1) (2019) 217–244, https://doi.org/10.1146/annurev-fluid-010518-040401.

[26] A. Håkansson, L. Brandt, Deformation and initial breakup morphology of viscous emulsion drops in isotropic homogeneous turbulence with relevance for emulsification devices, Chem. Eng. Sci. 253 (2022), 117599, https://doi.org/10.1016/j.ces.2022.117599.

[27] A. Håkansson, M. Crialesi-Esposito, L. Nilsson, L. Brandt, A criterion for when an emulsion drop undergoing turbulent deformation has reached a critically deformed state, Colloids Surf. A Physiochem. Eng. Asp. 648 (2022), 129213, https://doi.org/10.1016/j.colsurfa.2022.129213.

[28] A.E. Komrakova, Single drop breakup in turbulent flow, Can. J. Chem. Eng. 97 (10) (2019) 2727–2739, https://doi.org/10.1002/cjce.23478.

[29] D. Qian, J.B. McLaughlin, K. Sankaranarayanan, S. Sundaresan, S. Kontomaris, Simulation of bubble breakup dynamics in homogenous turbulence, Chem. Eng. Commun. 193 (2006) 1038–1063, https://doi.org/10.1080/00986440500354275.

[30] A. Rivière, W. Mostert, S. Perrard, L. Deike, Sub-Hinze scale bubble production in turbulent bubble break-up, J. Fluid Mech. 917 (2021) A40, https://doi.org/10.1017/jfm.2021.243.

[23] A. Baraldi, M.S. Dodd, A. Ferrante, A mass-conserving volume-of-fluid method: volume tracking and droplet surface-tension in incompressible isotropic turbulence, Comput. Fluids 96 (2014) 322–337, https://doi.org/10.1016/j.compfluid.2013.12.018.

[31] C. Shao, K. Luo, Y. Yang, J. Fan, Direct numerical simulation of droplet breakup in homogeneous isotropic turbulence: the effect of the Weber number, Int. J. Multiph. Flow. 107 (2018) 263–274, https://doi.org/10.1016/j.ijmultiphaseflow.2018.06.009.

[32] Toschi, F., Perlekar, P., Biferale, L., Sbragaglia, M. , (2010), Droplet Breakup in Homogeneous and Isotropic Turbulence. https://doi.org/10.48550/ARXIV.1010.1795.

[33] A. Vela-Martín, M. Avila, Deformation of drops by outer eddies in turbulence, J. Fluid Mech. 929 (2021) A38, https://doi.org/10.1017/jfm.2021.879.

[24] M. Crialesi-Esposito, M.E. Rosti, S. Chibbaro, L. Brandt, Modulation of homogeneous and isotropic turbulence in emulsions, J. Fluid Mech. 940 (2022) A19, https://doi.org/10.1017/jfm.2022.179.

[25] J.J. Derksen, H.E.A. Van Den Akker, Multi-scale simulations of stirred liquid–liquid dispersions, Chem. Eng. Res. Des. 85 (5) (2007) 697–702, https://doi.org/10.1205/cherd06161.

[34] J. Li, Y.Y. Renardy, M. Renardy, Numerical simulation of breakup of a viscous drop in simple shear flow through a volume-of-fluid method, Phys. Fluids 12 (2) (2000) 269–282, https://doi.org/10.1063/1.870305.

[35] A. Roccon, M. De Paoli, F. Zonta, A. Soldati, Viscosity-modulated breakup and coalescence of large drops in bounded turbulence, Phys. Rev. Fluids 2 (8) (2017), 083603, https://doi.org/10.1103/PhysRevFluids.2.083603.

[36] L. Scarbolo, F. Bianco, A. Soldati, Coalescence and breakup of large droplets in turbulent channel flow, Phys. Fluids 27 (7) (2015), 073302, https://doi.org/10.1063/1.4923424.

[37] L. Scarbolo, F. Bianco, A. Soldati, Turbulence modification by dispersion of large deformable droplets, Eur. J. Mech. B/Fluids 55 (2016) 294–299, https://doi.org/10.1016/j.euromechflu.2015.10.002.

[38] M.E. Rosti, F. De Vita, L. Brandt, Numerical simulations of emulsions in shear flows, Acta Mech. 230 (2) (2019) 667–682, https://doi.org/10.1007/s00707-018-2265-5.

[39] M.E. Rosti, Z. Ge, S.S. Jain, M.S. Dodd, L. Brandt, Droplets in homogeneous shear turbulence, J. Fluid Mech. 876 (2019) 962–984, https://doi.org/10.1017/jfm.2019.581.

[40] I. Bagkeris, V. Michael, R. Prosser, A. Kowalski, Modeling drop breakage using the full energy spectrum and a specific realization of turbulence anisotropy, AIChE J. 67 (7) (2021), e17201, https://doi.org/10.1002/aic.17201.

[41] P. Olad, M. Crialesi Esposito, L. Brandt, F. Innings, A. Håkansson, A direct numerical simulation investigation of the one-phase flow in a simplified emulsification device, J. Fluids Eng. 144 (8) (2022), 081209, https://doi.org/10.1115/1.4053896.

[42] M. Schmitt, H. Stark, Marangoni flow at droplet interfaces: three-dimensional solution and applications, Phys. Fluids 28 (1) (2016), 012106, https://doi.org/10.1063/1.4939212.

[43] E.A. Shevchenko, S. Mitra, S.A. Ermakov, A.G. Titov, A.A. Ermakov, P.S. G. Pattader, Joint mass transfer of two components associated with the

spontaneous interfacial convection in the liquid-liquid extraction system, Chem. Eng. Sci. 195 (2019) 301–311, https://doi.org/10.1016/j.ces.2018.09.018.

[44] R. Skartlien, K. Furtado, E. Sollum, P. Meakin, I. Kralova, Lattice–Boltzmann simulations of dynamic interfacial tension due to soluble amphiphilic surfactant, Phys. A Stat. Mech. Appl. 390 (2011) 2291–2302, https://doi.org/10.1016/j.physa.2011.02.022.

[45] P. Costa, A FFT-based finite-difference solver for massively-parallel direct numerical simulations of turbulent flows, Comput. Math. Appl. 76 (8) (2018) 1853–1862, https://doi.org/10.1016/j.camwa.2018.07.03.

[46] P.D. Mininni, A. Alexakis, A. Pouquet, Large-scale flow effects, energy transfer, and self-similarity on turbulence, Phys. Rev. E 74 (1) (2006), 016303, https://doi.org/10.1103/PhysRevE.74.016303.

[47] D. Vallefuoco, A. Naso, F.S. Godeferd, Small-scale anisotropy induced by spectral forcing and by rotation in non-helical and helical turbulence, J. Turbul. 19 (2) (2018) 107–140, https://doi.org/10.1080/14685248.2017.1400667.

[48] L. Davidson, M. Billson, Hybrid LES-RANS using synthesized turbulent fluctuations for forcing in the interface region, Int. J. Heat. Fluid Flow. 27 (6) (2006) 1028–1042, https://doi.org/10.1016/j.ijheatfluidflow.2006.02.025.

[49] P. Olad, M. Crialesi Esposito, L. Brandt, F. Innings, A. Håkansson, Towards best practice recommendations for turbulence modelling of high-pressure homogenizer outlet chambers – numerical validation using DNS data, Chem. Eng. Sci. 258 (2022), 117748, https://doi.org/10.1016/j.ces.2022.117748.

[50] S. Ii, K. Sugiyama, S. Takeuchi, S. Takagi, Y. Matsumoto, F. Xiao, An interface capturing method with a continuous function: the THINC method with multi-dimensional reconstruction, J. Comput. Phys. 231 (5) (2012) 2328–2358, https://doi.org/10.1016/j.jcp.2011.11.038.

[51] N. Vankova, S. Tcholakova, N.D. Denkov, I. Ivanov, V.D. Vulchev, T. Danner, Emulsification in turbulent flow 1. Mean and maximum drop diameters in inertial and viscous regimes, J. Colloid Interface Sci. 312 (2007) 363–380, https://doi.org/10.1016/j.jcis.2007.03.059.

[52] J. Solsvik, S. Maaß, H.A. Jakobsen, Definition of the single drop breakup event, Ind. Eng. Chem. Res. 55 (10) (2016) 2872–2882, https://doi.org/10.1021/acs.iecr.6b00591.

[53] H. Lamb. Hydrodynamics, sixth ed., Cambridge University Press, Cambridge, UK, 1932.

[54] B. Lalanne, O. Masbernat, F. Risso, A model for drop and bubble breakup frequency based on turbulence spectra, AIChE J. 65 (1) (2019) 347–359, https://doi.org/10.1002/aic.16374.

[55] C.A. Miller, L.E. Scriven, The oscillations of a fluid droplet immersed in another fluid, J. Fluid Mech. 32 (3) (1968) 417–435, https://doi.org/10.1017/S0022112068000832.

[56] H. Zhou, X. Yu, B. Wang, S. Jing, E. Lan, S. Li, Modeling study on drop breakup time in turbulent dispersions, Chem. Eng. Sci. 238 (2021), 116599, https://doi.org/10.1016/j.ces.2021.116599.